*Cerebral Cortex*, August 2019; 3561–3576

**doi: 10.1093/cercor/bhy231**
Advance Access Publication Date: 1 October 2018
Original Article

ORIGINAL ARTICLE

# Altered White Matter Organization in the TUBB3 E410K Syndrome

P. Ellen Grant[1,2,3], Kiho Im[2,3], Banu Ahtam[2,3], Cynthia T. Laurentys[2,3], Wai-Man Chan[3,4,5,6], Maya Brainard[3,4,5], Sheena Chew[3,4,5,6,9], Marie Drottar[2], Caroline D. Robson[1,3], Irene Drmic[7] and Elizabeth C. Engle[3,4,5,6,8]

[1]Department of Radiology, Boston Children's Hospital, Boston, MA 02115, USA, [2]Department of Pediatrics, Boston Children's Hospital, Boston, MA 02115, USA, [3]Harvard Medical School, Boston, MA 02115, USA, [4]Department of Neurology, Boston Children's Hospital, Boston, MA 02115, USA, [5]F.M. Kirby Neurobiology Center, Boston Children's Hospital, Boston, MA 02115, USA, [6]Howard Hughes Medical Institute, Chevy Chase, MD 20815, USA, [7]Hamilton Health Sciences, Ron Joyce Children's Health Centre, Hamilton, Ontario L8L 0A4, Canada, [8]Department of Ophthalmology, Boston Children's Hospital, Boston, MA 02115, USA and [9]Present address: Departments of Neurology, Brigham and Women's Hospital, Massachusetts General Hospital, and Harvard Medical School, Boston, MA 02115, USA

Address correspondence to P. Ellen Grant (Ellen.Grant@childrens.harvard.edu) and Elizabeth C Engle (Elizabeth.Engle@childrens.harvard.edu)

## Abstract

Seven unrelated individuals (four pediatric, three adults) with the TUBB3 E410K syndrome, harboring identical de novo heterozygous *TUBB3* c.1228 G>A mutations, underwent neuropsychological testing and neuroimaging. Despite the absence of cortical malformations, they have intellectual and social disabilities. To search for potential etiologies for these deficits, we compared their brain's structural and white matter organization to 22 controls using structural and diffusion magnetic resonance imaging. Diffusion images were processed to calculate fractional anisotropy (FA) and perform tract reconstructions. Cortical parcellation-based network analysis and gyral topology-based FA analyses were performed. Major interhemispheric, projection and intrahemispheric tracts were manually segmented. Subjects had decreased corpus callosum volume and decreased network efficiency. While only pediatric subjects had diffuse decreases in FA predominantly affecting mid- and long-range tracts, only adult subjects had white matter volume loss associated with decreased cortical surface area. All subjects showed aberrant corticospinal tract trajectory and bilateral absence of the dorsal language network long segment. Furthermore, pediatric subjects had more tracts with decreased FA compared with controls than did adult subjects. These findings define a TUBB3 E410K neuroimaging endophenotype and lead to the hypothesis that the age-related changes are due to microscopic intrahemispheric misguided axons that are pruned during maturation.

**Key words:** arcuate fasciculus (AF), autism, cingulum (Cing), corpus callosum (CC), corticospinal tract (CST), diffusion imaging, dorsal language network (DLN), genetics, inferior fronto-occipital fasciculus (IFOF), inferior longitudinal fasciculus (ILF), intellectual disability, magnetic resonance imaging (MRI), medial lemniscus (ML), misguidance, structural connectivity, superior longitudinal fasciculus (SLF), tractography, TUBB3, TUBB3 E410K syndrome, uncinate fasciculus (UF), ventral language network (VLN)

## Introduction

Microtubules are the major component of a cell's cytoskeleton; they are dynamic structures that grow and shrink, provide the track along which motor proteins move, and are believed to be critical for mitoses, neuronal migration, and axonal growth cone guidance during brain development (Keays et al. 2007; Tischfield et al. 2010). Microtubules are composed of polymers of heterodimers, each of which contains one α- and one β-tubulin isotype. Each tubulin isotype is encoded by a distinct gene (Lopata and Cleveland 1987), and heterozygous missense mutations in a subset of tubulin genes can result in neurodevelopmental disorders. The relative contributions of altered mitoses, migration, and axonal guidance to the neurodevelopmental disorder associated with a given tubulin mutation are, however, not well defined.

TUBB3 is the only neuronal-specific β-tubulin isotype and is expressed in all developing and mature neurons in the central and peripheral nervous system. *TUBB3* missense mutations have been identified in two patient cohorts. First, at least seven unique *TUBB3* missense mutations have been identified in children with developmental delay secondary to primary malformations of cortical development (MCDs) in the absence of cranial or spinal nerve deficits (Poirier et al. 2010; Bahi-Buisson et al. 2014; Oegema et al. 2015; Radmanesh et al. 2015). Second, 10 unique *TUBB3* missense mutations have been identified in children and adults with congenital fibrosis of the extraocular muscles (CFEOM), a complex congenital paralytic eye movement disorder of ptosis and restricted eye movements believed to arise from cranial nerve misguidance (Tischfield et al. 2010; Chew et al. 2013; Whitman et al. 2016). While several of these 10 CFEOM *TUBB3* mutations cause an isolated eye movement disorder, most cause mutation-specific syndromic forms of CFEOM that can include various combinations of additional cranial nerve dysfunction, progressive peripheral neuropathy, as well as social and intellectual disabilities, typically in the absence of magnetic resonance imaging (MRI)-detectable MCD. The etiology of intellectual and social disabilities resulting from CFEOM-TUBB3 mutations is unknown.

We previously reported a series of individuals harboring a de novo heterozygous *TUBB3* c.1228 G>A missense mutation that results in a TUBB3 E410K amino acid substitution and causes increased microtubule stability and reduced kinesin motor protein transport (Tischfield et al. 2010; Niwa et al. 2013; Ti et al. 2016). These patients had remarkably similar phenotypes, with congenital dysfunction of multiple cranial nerves resulting in CFEOM3, Kallmann syndrome (anosmia and hypogonadotropic hypogonadism), and facial weakness, as well as an early adult-onset progressive axonal polyneuropathy and intellectual and social disabilities (Chew et al. 2013). Structural MRI revealed thinning to the absence of the corpus callosum (CC), anterior commissure (AntC), olfactory bulbs, oculomotor nerves, and facial nerves with hypoplastic to absent olfactory sulci. These subjects also had a paucity of white matter and, as with most CFEOM-TUBB3 mutations, no MRI-detectable MCD (Tischfield et al. 2010; Chew et al. 2013). We also found that *Tubb3* mutant mouse embryos harboring the human R262C CFEOM disease-causing amino acid substitution have agenesis of the CC with Probst bundles and thin and tortuous to absent AntC, as well as defects in the guidance and branching of the oculomotor, trochlear, and trigeminal nerves (Tischfield et al. 2010). Together, the small or absent CC and AntC and the paucity of white matter in TUBB3 E410K humans, combined with absent CC and AntC and aberrant cranial nerve trajectories in the phenotypically similar R262C mice, support central axon misguidance as a potential cause of social and intellectual disabilities in TUBB3 E410K humans.

The recurrence of the de novo *TUBB3* c.1228 G>A missense mutation and its manifestation as the fully penetrant TUBB3 E410K human syndrome provides an opportunity to compare white matter organization within this genetically homogeneous cohort and to ask if the TUBB3 E410K substitution results in stereotypical defects in central axonal guidance. By comparing children with adults, potential changes that occur with development can also be explored. Toward these goals, we performed neuropsychological analyses, MRI, and diffusion tensor imaging (DTI) in four children and three adults with the TUBB3 E410K syndrome, followed by unbiased whole-brain connectivity analysis (Sporns et al. 2005), gyral topology-based FA analysis of short-, mid-, and long-range connectivity (Hagmann et al. 2010; Shukla et al. 2011; Im et al. 2014, 2016) and hypothesis-based manual segmentation and analysis of major white matter tracts.

## Materials and Methods

### Subjects and Controls

Seven unrelated individuals participated in this study (4 children aged 7–10 years and 3 adults aged 21–26 years, referred to as "subjects" and ordered in ascending age from subject S1 to S7), each of whom harbored a de novo heterozygous *TUBB3* c.1228 G>A missense mutation (p.E410K). Informed consent was obtained from all subjects and/or their parents/guardians in accordance with the requirements of the Boston Children's Hospital (BCH) Institutional Review Board (IRB). Detailed clinical phenotypes and genetic data for all subjects except S4, as well as structural MRI for all subjects except S3 and S4 were previously reported (Tischfield et al. 2010; Chew et al. 2013). S4's history and physical exam features were obtained from parental interviews, medical records, and examinations at BCH, and his *TUBB3* mutation detection, confirmation of maternity and paternity, and determination of de novo status were performed from salivary DNA as previously described (Tischfield et al. 2010).

Structural and DTI data from 22 age- and sex-matched typically developing individuals served as controls (10 children and 12 adults, referred to as "controls"). The pediatric (ordered in ascending age as PC1-PC10) and adult (ordered in ascending age as AC1-AC12) control groups were selected from BCH clinical and Massachusetts General Hospital (MGH) research archives, respectively, with appropriate IRB approval. The following inclusion criteria were used for pediatric controls: 1) between 7 and 13 years of age when neuroimaging was obtained; 2) presented for evaluation of headache and were reported by a pediatric neurologist to otherwise have a normal neurological history and examination; 3) had undergone structural and diffusion MRI examinations of the brain performed at 3.0 Tesla (T) with a similar protocol to the exam performed in the TUBB3 E410K pediatric subject group; 4) structural and diffusion MRI was read as normal by a clinical pediatric neuroradiologist; 5) no significant imaging artifacts were present in the neuroimaging data. The following inclusion criteria were used for adult controls: 1) between the ages of 22–30 years when neuroimaging was obtained; 2) a history of neurological or psychiatric condition had been excluded; 3) had undergone structural and diffusion MRI examination of the brain performed at 3.0 T with the same protocol as the TUBB3 E410K adult participation

group; 4) no incidental findings were noted on structural and diffusion MRI; 5) no significant imaging artifacts were present in the neuroimaging data. For analysis, subjects and controls were divided into pediatric and adult groups to account for age-dependent qualitative and quantitative changes.

## Neuropsychological Assessments

Subjects S3, S4, S5, and S7 had neuropsychological testing specifically for this study, as described in Supplementary Material. Neuropsychological test results for subjects S1, S2, and S6 were obtained from medical records and varied in the specific tests administered.

## Structural and Diffusion MRI Data Acquisition

All structural and diffusion MRI scans were acquired on 3.0 T Siemens whole-body MR scanners (Tim Trio) equipped with a 32-channel head coil. General data acquisition parameters are summarized in the following.

Adult and pediatric subject data acquisition at BCH: 1) Structural imaging MPRAGE sequence: $1 \times 1 \times 1$ mm$^3$; repetition time (TR) = 2270–2530 ms; echo time (TE) = 1.56–1.74 ms; inversion time (TI) = 1300–1450 ms; flip angle = 7°. 2) Diffusion imaging sequence: $2 \times 2 \times 2$ mm$^3$; TR = 8000–8800 ms; TE = 83–84 ms; 10 images acquired with $b = 0$; 60 diffusion directions at $b = 700$ s/mm$^2$. Data from one subject (S1) were acquired with $2 \times 2 \times 2$ mm$^3$; TR = 9100 ms; TE = 88 ms; 10 images acquired with $b = 0$; 30 diffusion directions at $b = 1000$ s/mm$^2$.

Pediatric control data acquisition at BCH: 1) Structural imaging MPRAGE sequence: $1 \times 1 \times 1$ mm$^3$; TR = 1540-2530 ms, TE = 1.66–3.39 ms; TI = 800–1450 ms; flip angle = 7–9°. 2) Diffusion imaging sequence: $2 \times 2 \times 2$ mm$^3$; TR = 7890–13 000 ms; TE = 88–91 ms; five images acquired with $b = 0$; 30 diffusion directions at $b = 1000$ s/mm$^2$.

Adult control data acquisition at MGH: 1) Structural imaging MPRAGE sequence: $1 \times 1 \times 1$ mm$^3$ or $1 \times 1 \times 1.2$ mm$^3$; TR = 2300 – 2530 ms; TE = 2.91–3.44 ms; TI = 900–1100 ms, flip angle = 7–9°. 2) Diffusion imaging sequence: $2 \times 2 \times 2$ mm$^3$; TR = 7300 – 7600 ms; TE = 79–82 ms; 10 images acquired with $b = 0$; 60 diffusion directions at $b = 700$ s/mm$^2$.

## Structural MRI Processing and Analysis

Structural MR images were processed using the FreeSurfer pipeline, which includes brain extraction, intensity nonuniformity correction, white matter and gray matter tissue segmentation, cortical surface reconstruction, and cortical/subcortical parcellation (surfer.nmr.mgh.harvard.edu) (Dale et al. 1999; Fischl et al. 1999, 2004). The accuracy of white/gray matter segmentation and subregion parcellation was inspected and confirmed visually. The following were extracted from the FreeSurfer output for each individual: 1) Total brain, white matter, cortical gray matter, and deep gray nuclei volumes; 2) cortical thickness; 3) inner cortical surface area; and 4) CC volume.

## Diffusion MRI Processing and Analysis

Diffusion images were first preprocessed to correct for minor eddy current distortions and motion using FMRIB software library (FSL) tools (http://www.fmrib.ox.ac.uk/fsl/fdt). All diffusion images in the series were aligned to the first b0 image using affine registration (Jenkinson et al. 2002). Head motion was estimated and quantified for each subject to test if the TUBB3 E410K subjects showed different head motion compared with controls. Average volume-by-volume translation and rotation were extracted from affine transformation of the diffusion volumes and a single value, total motion index (TMI), was calculated (Yendiki et al. 2013).

Diffusion tensor models were estimated and the diffusion measures of fractional anisotropy (FA) and mean diffusivity (MD), radial diffusivity (RD), and axial diffusivity (AD) were calculated at each voxel (Basser et al. 1994). The motion- and eddy current-corrected raw diffusion data were then processed through the interpolated streamline algorithm (Lazar 2010) within the Diffusion Toolkit software to create white matter tracts (trackvis.org) (Wang et al. 2007). Tracts were terminated either when the angle between two consecutive orientation vectors was greater than a threshold of 45° or when fibers extended outside of the brain surface.

### *Whole-Brain Analysis of Diffusion Metrics*

The first b0 images were coregistered onto the T1-weighted images using FSL's intensity-based affine registration tool, FLIRT (www.fmrib.ox.ac.uk/fsl/flirt). Using the inverse transform, the white matter volumes segmented by FreeSurfer were transformed to the diffusion image space. Mean values of FA, MD, RD, and AD in the whole-brain white matter were measured with the use of a binary mask for the white matter. To confirm that aberrant diffusion tensor-based tracts could not arise erroneously due to image noise and reduced tract anisotropy, artificial noise was added to the images of controls to determine if this resulted in images similar to those of the subjects. Gaussian white noise of mean zero was added to the raw diffusion-weighted images. The variance of noise was determined as 0.1%, 0.5%, and 1% of maximum intensity range, and then tracts were reconstructed for each group. The overall directionality of the tracts was visually inspected to estimate the effect of noise on tractography and compared with the tracts of subjects.

### *FreeSurfer Parcellation-based FA and Network Analysis*

To assess whole-brain white matter connectivity in an unbiased and nonhypothesis-driven manner, a human brain connectome approach was used, which models the whole-brain network with a graph using a set of nodes and interconnecting edges (Sporns et al. 2005). To define the nodes of a brain graph, we obtained 68 cortical regions using the automatic cortical parcellation provided by FreeSurfer (Fischl et al. 2004; Desikan et al. 2006). Two node regions were considered to have a structural connection (edge) when the endpoints of fiber tracts were located <3 mm from each of the two regions (Im et al. 2014). Edge number was determined by the number of streamlines connecting two nodes (Hagmann et al. 2010). The mean FA value along all the fibers connecting each pair of cortical regions (each edge connection) was measured and FA-weighted structural connectivity network was examined in the whole brain.

To assess global topological organization of the network, graph theoretical analysis was performed on the weighted connectivity network for subjects and controls using the Brain Connectivity Toolbox (Rubinov and Sporns 2010). We computed the weighted clustering coefficient and transitivity as measures of network functional segregation (Onnela et al. 2005). The average shortest path length between all pairs of nodes in the network or characteristic path length of the network (Watts and Strogatz 1998) and global efficiency (Latora and Marchiori 2001) were also calculated. The graph measures were scaled

against the mean values of graph measures obtained from 1000 matched random graphs that preserved the same number of nodes, edges, and degree sequence (Maslov and Sneppen 2002). Following the analysis of the global network organization, we compared the FA values between subjects and controls for each connection between two regions in the network.

#### *Gyral Topology-based FA Analysis*

To enable an unbiased assessment of short-, middle-, and long-range connections, we repeated the connectivity analysis with nodes defined using the individual's gyral folding patterns (Im et al. 2014, 2016). First, FreeSurfer was used to compute the depths of cortical sulci (Fischl et al. 1999), and a watershed image process was performed based on the sulcal depth map to define gyral topology-based node regions on the white matter surface (Im et al. 2014). To prevent overextraction of the noisy gyral segments, the noise of the depth map was reduced with surface-based heat kernel smoothing with a full-width half-maximum value of 10 mm (Chung et al. 2005). In addition, segment merging was performed in the watershed algorithm using the area of the segment. Small regions below the area threshold of 30 $mm^2$ were merged into adjacent gyral regions (Im et al. 2010, 2014). After the gyral-based parcellation, edge connections between two gyral regions were defined using the same method as described above. Different tract groups were then constructed according to individual gyral pattern and topology (Im et al. 2014, 2016). We determined the shortest topological path between any two gyral segments and defined them as first through fourth and higher neighbors as follows: gyral segments adjacent to one another were defined as first neighbors, and gyral segments separated by one, two, or three or more gyral segments were defined as second, third, and fourth or higher neighbors, respectively. As a final step, mean FA was measured for the fiber tract connections (or edges) between the first (short-range), second and third (middle-range), and fourth and higher (long-range) neighboring gyri. First neighbor gyri were then interpreted as short association U-fiber connections, second and third neighbor gyri as neighborhood intrahemispheric association fiber connections, and fourth and higher neighbor gyri as long intrahemispheric association fiber connections.

#### *Manual Tract Segmentation and FA Analysis*

To investigate the potential specific tract abnormalities in the subjects, representative sets of fiber tracts were manually segmented. These included the commissural/interhemispheric CC fibers, the bilateral projection fibers (PFs) of the corticospinal tracts (CSTs) and medial lemniscus (ML), and the association fibers of the cingulum (Cing) as well as the bilateral pathways of the dorsal and ventral language networks (DLN and VLN, respectively). The DLN included three pathways: anterior segment (DLN.ant), long segment (DLN.long), and posterior segment (DLN.post). The VLN also included three pathways: inferior fronto-occipital fasciculus (VLN.IFOF), inferior longitudinal fasciculus (VLN.ILF), and uncinate fasciculus (VLN.UF).

Tracts were manually segmented with the use of the TrackVis software (TrackVis.org) by placing region of interest (ROI) filters according to the segmentation procedure outlined by Catani and de Schotten (Catani and Thiebaut de Schotten 2008) and Wakana (Wakana et al. 2004) and/or based on the location of well-established anatomical landmarks through which the segmented tracts pass (Schmahmann and Pandya 2009). ROIs were placed on combinations of color FA maps, noncolor FA maps, ADC maps, and b0 anatomical images in order to increase accuracy of tract segmentation. As each ROI was placed, the resulting tracts were evaluated for anticipated biologically improbable fibers. Tracts which were considered biologically improbable were manually removed in both controls and subjects, according to the following criteria: 1) fibers that looped back on themselves, 2) fibers that jumped to a known adjacent pathway, 3) fibers that were too short to form a coherent tract, 4) tracts that had too few fibers (<10). Tracts were reconstructed in both hemispheres. The CC was divided into five equal segments and 3DSlicer's SlicerDMRI project (dmri.slicer.org) (Norton et al. 2017) was used to view the CC organization using both ellipsoids and tracts. Fibers passing through the cerebral peduncle and into superior–inferior-orientated tracts in the midpons were considered a part of the descending CST. Fibers passing through other regions of the midbrain from superior–inferior-oriented tracts in the midpons were considered a part of the ascending ML. For full details on ROI placement, please see Supplementary Material.

The size, presence or absence, and general direction of each tract were qualitatively assessed and group comparisons of FA values for each tract were performed.

### Statistical Analyses

Comparison of subjects and controls for sex was computed using Fisher's exact test. Because of the small sample size of the subject cohort, the Mann–Whitney *U* test, a nonparametric two-group statistical analysis, was performed for the remaining between-group (pediatric subjects vs. pediatric controls; adult subjects vs. adult controls) and within-group (pediatric vs. adult subjects; pediatric vs. adult controls) comparisons. Between-group comparisons included age at the time of neuroimaging, TMI, whole-brain and regional structural measures, whole-brain white matter mean FA, MD AD, and RD, FA-weighted structural connectivity measures, mean FA of tracts connecting FreeSurfer defined parcellations, mean FA of tracts connecting gyral-based parcellations, and mean FA of manually segmented tracts of interest. Within-group comparisons were performed on the measures showing statistical significance on between-group analysis to determine if these differences were not driven by within-group differences. Equality of variance in the FA measures between pediatric and adults of both subject and control groups was assessed using Levene's test to determine if differences in FA variance could be contributing to between-group differences. False discovery rate control (FDR) was used for adjusting the statistical results for multiple group comparisons at a *q*-value (FDR adjusted/corrected *P* value) of 0.05 (Benjamini and Hochberg 1995; Genovese et al. 2002).

## Results

### Participant Demographics

Subjects S1–S3 and S5–S7, who are from diverse ethnic and geographic backgrounds, were each previously reported to harbor a heterozygous de novo *TUBB3* c.1228 G>A mutation and to manifest the corresponding TUBB3 E410K clinical syndrome (Tischfield et al. 2010; Chew et al. 2013). Subject numbers in the current study correspond to Chew et al. (2013) as follows (current study: Chew et al.): S1:II, S2:I, S3:III, S5:VI, S6:VII, S7:VIII. Subject S4, who was not previously published, also presented clinically with the TUBB3 E410K syndrome (Supplementary Material) and harbored a heterozygous *TUBB3* c.1228 G>A mutation (p.E410K) that was absent in the DNA of his biological parents (Supplementary Fig. 1A,B). Table 1 provides the TUBB3 E410K subjects' sex and

**Table 1** Participant demographics and neuropsychological testing results

| Subject, Sex | Age at MRI scan<br>NP testing (y:m) | IQ classification FSIQ, SS (%ile) | Language (%ile) | | | Adaptive functioning (%ile) | ASD diagnosis | Emotional or behavioral concerns | | | | |
|---|---|---|---|---|---|---|---|---|---|---|---|---|
| | | | Total | Expressive | Receptive | | | INT | EXT | ATT | OCP | SOM |
| **Pediatric Subjects** | | | | | | | | | | | | |
| 1, M[b] | 7:11<br>12:4 | ID (1%-37%) | — | 106^ (66%) | — | (3%) | Non-ASD (symptoms present) | N | N | N | — | — |
| 2, F | 9:6<br>9:2 | Low avg 84 (14%) | — | — | — | — | Non-ASD | N | N | N | — | N |
| 3, F | 9:9<br>8:3[a] | Low avg 81 (10%) | Mod-severe (0.5 %) | 6% | <0.1% | Ex low (1%) | ASD | N | Y | Y | N | N |
| 4, M | 10:9<br>11:2[a] | Ex low, mild ID 51 (0.05%) | Mod-severe (0.5%) | 2% | 0.3% | Ex low (0.1%) | ASD (Asperger) | Y | N | Y | Y | Y |
| **Adult Subjects** | | | | | | | | | | | | |
| 5, M | 20:6<br>19:2[a] | Ex low 66 (1%) | Mod-severe (1%) | 2% | 3% | — | ASD | Y | N | Y | — | — |
| 6, M | 21:1<br>18:1 | Ex low, mild ID 59 (0.3%) | Below age expectations | | | Ex low (<1%) | ASD | Y | Y | Y | — | Y |
| 7, M[c] | 26:4[a] | — | — | — | — | — | Non-ASD (symptoms present) | N | N | N | Y | N |

Note: — = data not available; M = male; F = female; y = year; m = month; ASD = autism spectrum disorder; ID = intellectual disability; FSIQ = Full Scale Intelligence Quotient; SS = standard score; % = percentile; avg = average; Mod = moderate; Ex = extremely; INT = internalization; EXT = externalization; ATT = attention deficit/hyperactivity problems; OCP = obsessive–compulsive problems; SOM = somatic problems; Y = yes; N = no. [a]Tested specifically for this study. [b]Subject 1 FSIQ was not available because of significant variability in intellectual profile ranging from the extremely low to average range, in part due to visual limitations. Subscales scores: verbal comprehension = 95 (37th percentile; Average); visual spatial = 86 (18th percentile; low average); fluid reasoning = 64 (first percentile; extremely low); working memory = 67 (first percentile; extremely low); processing speed = 66 (first percentile; extremely low). [c]Neuropsychological testing was not completed because subject 7 did not speak English. ^based on expressive one-word picture vocabulary (EVT, fourth edition), not a more comprehensive measure of expressive language abilities.

age at the time of neuroimaging and neuropsychiatric testing. Comparisons of subjects and controls for sex and mean age at the time of neuroimaging revealed no significant differences (sex: children $P = 1.000$, adults $P = 1.000$; age: children $P = 1.000$, adults $P = 0.334$).

## Neurological and Neuropsychological Assessments

Each subject was diagnosed clinically and genetically with the TUBB3 E410K syndrome (Chew et al. 2013), manifesting as CFEOM, facial weakness, Kallmann syndrome, intellectual and social disabilities, and in some cases vocal cord paralysis, tracheomalacia, and cyclic vomiting. Each had normal motor bulk, strength, tone and reflexes, and normal sensory examinations as children. Adult subjects developed a progressive sensorimotor polyneuropathy. S2 had complex partial seizures.

Neuropsychological test results for each participant are summarized in Table 1. An assessment of intellectual abilities was completed in six of seven subjects, although an overall IQ standard score was not calculated for S1 due to significant variability in performance (i.e., ranging from average to extremely low range). The overall IQ standard scores ranged from 51 to 84, and three individuals were diagnosed with mild intellectual disability based on IQ profile and deficits in adaptive functioning. An assessment of overall language skills (including receptive and expressive language) was completed in S3, S4, S5, and S6, and all had language impairments that fell within the moderate to severe range. An assessment of expressive vocabulary was completed in S1, indicating average vocabulary skills. An assessment of adaptive functioning (i.e., independence skills) was completed in S1, S3, S4, and S6 and was below age expectations in all, including one subject without intellectual disability.

Four of the subjects were diagnosed with autism spectrum disorder (ASD). Although S1 and S7 were not diagnosed with ASD, ASD symptoms were noted. Specifically, S1 frequently repeated word and phrases spoken by others (i.e., echolalia), frequently clapped his hands, and had linear and goal-directed thought processes. S7 had lack of flexibility/rigid behavior, repetitive/compulsive behaviors, and difficulty with perspective taking (i.e., poor theory of mind). In addition, a summary of emotional and behavioral concerns obtained using a variety of standard measures and information gathered from parent interviews raised concerns about attention problems (ATT) in four individuals, internalizing (INT) in three, and obsessive–compulsive problems (OCP), somatic complaints (SOM), and externalizing (EXT) each in two.

## Structural MRI

### *Qualitative*

Volumetric T1- and axial T2-weighted images from S3 and S4 (Supplementary Fig. 1C–J) were similar to the structural MR imaging previously reported for S1, S2, and S5–S7 (Tischfield et al. 2010; Chew et al. 2013). The CC was small in caliber and extent, olfactory sulci were absent and olfactory bulbs were hypoplastic to absent. The basal ganglia appeared normal and no MCDs were evident. The AntC was hypoplastic or not visible on the structural images, while it was consistently visible on the T1 axial images of all controls. Cranial nerve imaging showed bilaterally absent oculomotor nerves and hypoplastic facial nerves.

### *Quantitative*

Consistent with qualitative review, pediatric and adult subjects had a significant reduction in CC volume (pediatric $P = 0.002$, adult $P = 0.004$) and no significant difference in cortical thickness or deep gray nuclei volume compared with controls (Table 2). In addition, significant reductions in whole-brain, cortical gray matter, and white matter volumes ($P = 0.004$, 0.018, and 0.004, respectively) and significant reductions in cortical surface area ($P = 0.004$) were found in adult subjects compared with adult controls. Notably, pediatric subjects did not have significant differences in these measures compared with pediatric controls.

## Diffusion MRI

### *Whole-Brain Analysis of Diffusion Metrics*

Group comparisons of TMI showed no significant differences between the TUBB3 E410K subjects and controls in pediatric ($P = 0.142$) and adult ($P = 0.070$) groups. When increasing noise (0.1%, 0.5%, and 1% variance of intensity range) was added to raw diffusion images, tract-based mean FA values decreased and tracts became increasingly shorter. This resulted in failure of reconstruction of long-range tracts but not in the reconstruction of aberrant tracts (Supplementary Fig. 2).

Notably, pediatric subjects S2, S3, and S4 as well as all adult subjects and all adult controls had diffusion MRI studies performed with $b = 700$ s/mm$^2$, while S1 as well all pediatric controls had diffusion MRI studies performed with $b = 1000$ s/mm$^2$. Therefore, $b$ values were on average lower for pediatric subjects compared with pediatric controls. Given that lower $b$ values result in higher MD (Melhem et al. 2000; Hui et al. 2010), the higher whole-brain MD and RD values for pediatric subjects ($P = 0.036$ and 0.008, respectively) are at least in part due to differences in b values. Thus, MD, RD, and AD values are reported in Supplementary Material but not used in additional analysis (Supplementary Table 1). FA is less dependent on $b$ value than is MD and has been reported to show little change with $b$ values between 500 and 1000 s/mm$^2$ (Melhem et al. 2000; Hui et al. 2010). Therefore, the significantly lower whole-brain FA values in pediatric subjects compared with controls ($P = 0.014$) is likely unaffected by different $b$ values. Moreover, the observation that pediatric subject 1, imaged with the same $b$ values as pediatric controls, has a lower whole-brain FA value compared with all pediatric controls supports the impression that the FA decreases observed in pediatric subjects are real (Supplementary Table 1). The FA differences in S1 were also present in the majority of the individual tract analyses and in gyral-based connectivity analysis discussed in the following. By contrast, no significant group differences were found in whole-brain FA, MD, RD, and AD in the adult subjects compared with adult controls (Supplementary Table 1). FA comparisons were included for both children and adults in the whole-brain- and tract-based analyses in the following.

### *FreeSurfer Parcellation-based FA Network Analysis*

Graph theoretical analysis of FA-weighted networks revealed significantly higher clustering coefficients ($P = 0.002$ and 0.009 for pediatric and adult subjects, respectively) as well as increased transitivity ($P = 0.002$ and 0.018 for pediatric and adult subjects, respectively). In network integration analysis, characteristic path length was significantly higher ($P = 0.036$ and 0.004 for pediatric and adult subjects, respectively) and global efficiency lower ($P = 0.024$ and 0.004 in pediatric and adult subjects, respectively). Statistical results for the group comparisons are presented in Table 3. FA values for each connection between two regions in the network were not statistically significant between the subjects and controls at the 0.05 level of FDR-corrected $P$.

**Table 2** Statistical results for the group comparisons of whole brain, cortical gray matter, white matter, and CC volumes ($mm^3$), cortical thickness (mm), and cortical surface area ($mm^2$) in pediatric and adult groups

| | Control | TUBB3 E410K | | P |
|---|---|---|---|---|
| Pediatric | | | | |
| Whole brain | 1 196 374.0 (115 682.5) | 1 071 493.5 (147 653.2)<br>[1 025 473, 957 321, 10 148 051 288 375] | – | 0.188 |
| Cortical gray matter | 577 592.9 (60 720.8) | 550 616.9 (72 825.1)<br>[538 023.3, 483 411.5, 527 068.1, 653 964.7] | – | 0.374 |
| Cortical thickness | 2.982 (0.282) | 3.152 (0.120)<br>[3.074, 3.025, 3.264, 3.244] | – | 0.374 |
| Cortical surface area | 167 393.0 (21 037.6) | 146 488.0 (17 087.4)<br>[146 464.6, 133 014.3, 135 869.0, 170 605.4] | – | 0.188 |
| White matter | 395 339.9 (58 145.2) | 338 966.8 (65 491.6)<br>[314 667.4, 291 328.6, 314 025.5, 435 845.8] | – | 0.304 |
| CC | 3025.6 (473.5) | 1 576.2 (240.7)<br>[1933.3, 1496.0, 1409.6, 1465.9] | ↓ | 0.002* |
| Deep gray matter | 49 637.4 (5565.8) | 42 818.8 (4429.5)<br>[42 960.4, 38 209.4, 41 337.1, 48 768.5] | – | 0.036 |
| Adult | | | | |
| Whole brain | 1 304 293.5 (70 474.8) | 1 034 269.3 (151 287.8)<br>[1 171 447, 8 720 071 059 354] | ↓ | 0.004* |
| Cortical gray matter | 602 590.6 (31 327.9) | 499 428.3 (81 908.6)<br>[575 754.4, 412 894.2, 509 636.2] | ↓ | 0.018* |
| Cortical thickness | 3.169 (0.101) | 3.069 (0.195)<br>[3.294, 2.940, 2.974] | – | 0.365 |
| Cortical surface area | 166 048.7 (8617.2) | 135 289.7 (14 226.1)<br>[144 862.8, 118 942.5, 142 063.8] | ↓ | 0.004* |
| White matter | 450 147.5 (32 842.2) | 343 225.8 (62 153.8)<br>[390 891.3, 272 927.0, 365 859.1] | ↓ | 0.004* |
| CC | 3343.2 (315.7) | 1 834.4 (224.5)<br>[2081.4, 1779.3, 1642.6] | ↓ | 0.004* |
| Deep gray matter | 53 923.6 (4012.0) | 46 690.6 (5421.6)<br>[50 787.2, 40 542.7, 48 742.0] | – | 0.048 |

Data: mean (standard deviation).
Data in []: individual values for all subjects (pediatric: [subjects 1, 2, 3, and 4], adult: [subjects 5, 6, and 7]).
*Corrected $P < 0.05$.

**Table 3** Statistical results for the group comparisons of graph measures based on FA-weighted network in pediatric and adult groups

| | Control | TUBB3 E410K | | P |
|---|---|---|---|---|
| Pediatric | | | | |
| Clustering coefficient | 2.284 (0.135) | 2.810 (0.214)<br>[2.995, 2.558, 2.707, 2.982] | ↑ | 0.002* |
| Transitivity | 2.018 (0.099) | 2.389 (0.133)<br>[2.508, 2.215, 2.358, 2.477] | ↑ | 0.002* |
| Characteristic path length | 1.094 (0.018) | 1.131 (0.029)<br>[1.154, 1.119, 1.095, 1.157] | ↑ | 0.036* |
| Global efficiency | 0.947 (0.008) | 0.928 (0.013)<br>[0.919, 0.932, 0.946, 0.916] | ↓ | 0.024* |
| Adult | | | | |
| Clustering coefficient | 2.362 (0.219) | 3.018 (0.163)<br>[3.008, 3.186, 2.859] | ↑ | 0.009* |
| Transitivity | 2.019 (0.192) | 2.473 (0.177)<br>[2.497, 2.637, 2.286] | ↑ | 0.018* |
| Characteristic path length | 1.088 (0.018) | 1.129 (0.008)<br>[1.129, 1.121, 1.136] | ↑ | 0.004* |
| Global efficiency | 0.950 (0.010) | 0.926 (0.004)<br>[0.928, 0.928, 0.922] | ↓ | 0.004* |

Data: mean (standard deviation).
Data in []: individual values for all subjects (pediatric: [subjects 1, 2, 3, and 4], adult: [subjects 5, 6, and 7]).
*Corrected $P < 0.05$

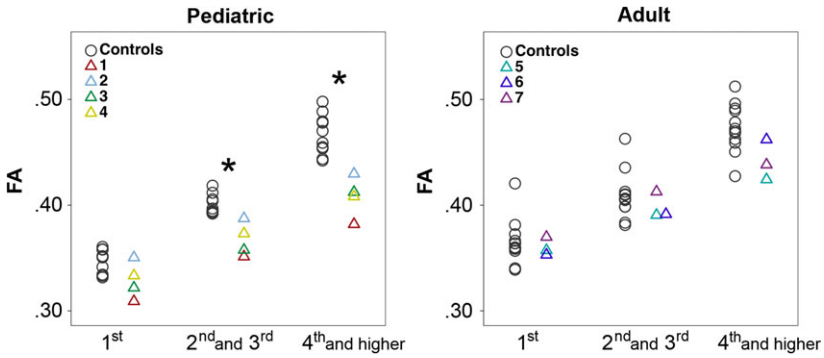


**Figure 1.** Gyral-based FA values. Scatter plots of FA value for the connections between the first (short-range), second and third (middle-range), and fourth and higher (long-range) neighboring gyri in pediatric and adult subjects versus controls (*corrected $P < 0.05$). Pediatric subjects have significantly lower FA in middle to long-range connections compared with pediatric controls, while adult subjects show no significant differences compared with adult controls.

### *Gyral Topology-based FA Analysis*

The unbiased gyral region parcellation provided a uniform and consistent segmentation of regions similar in size and gyral topology. The pediatric subjects had significantly decreased FA values for second and third neighboring gyri, interpreted as neighborhood association fiber connections, and for fourth and higher gyral neighbor connections, interpreted as long intrahemispheric association fiber connections, compared with pediatric controls ($P = 0.002$ and 0.002, respectively) (Fig. 1), but not for the first neighboring gyri, regarded as short association U-fiber connections. The adult subjects did not show significantly different FA values compared with adult controls for all gyral neighbor connections (Fig. 1).

In pediatric and adult group comparisons, the pediatric controls showed significantly lower FA values for first neighboring gyral connections compared with adult controls ($P = 0.009$), but not for all other gyral neighbor connections. In the test for an equality of variance, the pediatric and adult groups did not show significant differences in variance of the FA values.

### *Manual Tract Segmentation and FA Analysis*

Pediatric subjects had significantly lower FA compared with pediatric controls (corrected $P < 0.05$) in the bilateral CST, bilateral ML, CC, right DLN.ant and DLN.post, bilateral VLN.IFOF, and bilateral Cing. Adult subjects had significantly lower FA compared with adult controls (corrected $P < 0.05$) in the bilateral CST, right ML, CC, bilateral DLN.ant, and bilateral VLN.IFOF (Fig. 2). In pediatric and adult group comparisons, neither the pediatric versus adult control groups (Supplementary Table 2) nor the pediatric versus adult subject groups (Supplementary Table 3) showed significantly different FA values or variance in FA values for all manually segmented tracts at the 0.05 level of FDR-corrected $P$. Thus, no significant within-group age-related changes in FA were noted in the manually segmented tracts. Qualitative assessment of these manually segmented tracts is presented by tract group below.

*CSTs and MLs*. The CST cross-sectional area in the pons (visualized as bilateral round blue regions in the anterior pons on color FA maps) was decreased in size and irregular in shape for all subjects compared with controls (Fig. 3, column A; Supplementary Fig. 3*A*,*B*, column A), with S4 and S6 showing the most dramatic differences. In addition, the ML in the pons (visualized as bilateral broader blue regions in the posterior pons on color FA maps) was dysmorphic in all subjects (Fig. 3, column A). In controls, tracts coursed from the perirolandic region through the ipsilateral cerebral peduncle and descended only through the ipsilateral anterior pons (Supplementary Fig. 3*A*,*B*, columns B and C). Note that artifacts in the midbrain significantly reduced the number of fibers that could be reconstructed in PC2 and the left CST was excluded from statistical analysis because the fiber number was < 10. In subjects, the fibers were more divergent with fewer fibers descending through the ipsilateral cerebral peduncle and anterior pons. Surprisingly, and unlike controls, a significant number of fibers coursed through the cerebral peduncle into the posterior pons, in the expected region of the ML (Fig. 3, columns B and C, rows 2–8).

Bilateral ML tracts (Fig. 3, columns D and E; Supplementary Fig. 3*A*,*B*, columns D and E) were reconstructed by placing inclusion ROIs in the anterior and posterior pons and exclusion ROIs in the ipsilateral cerebral peduncle in all participant groups. When inclusion ROIs were placed both in the posterior pons and the cerebral peduncle, as anticipated, no tracts were observed in any of the control participants (Supplementary Fig. 3*A*,*B*, columns F and G); by contrast, in all subjects except in the left hemisphere of S5, there were bilateral tracts with variable fiber number passing through these ROIs (Fig. 3, columns F and G).

In pediatric subjects, both the CST and ML had significantly reduced FA values compared with controls in both left (CST and ML with $P = 0.003$ and 0.002, respectively) and right ($P = 0.002$ and 0.002) hemispheres (Fig. 2). In adult subjects, bilateral CST ($P = 0.018$ for left CST and $P = 0.004$ for right CST) and right ML ($P = 0.004$) had significantly reduced FA values compared with controls (Fig. 2).

*Corpus Callosum*. Fewer CC fibers were reconstructed in subjects compared with controls (Fig. 4, columns A, C, and E; Supplementary Fig. 4*A*,*B*), and the reconstructed tracts showed variable connectivity to the temporal, parietal, and occipital regions, likely due to the reduction in size and variable reduction in extent of the CC which can be seen on the structural scans (Supplementary Fig. 1*C*,*G*; (Chew et al. 2013)). Exploration of the CC organization using fibers and glyphs (Fig. 4, columns B and D) revealed varying degrees of disorganization with a suggestion of heterotopic connections in S5. The CC had significantly reduced FA values compared with controls in both pediatric ($P = 0.002$) and adult subjects ($P = 0.004$, Fig. 2).

*Dorsal Language Network*. The DLN.ant was present in all pediatric and adult subjects except for S1 bilaterally, but it was diminutive in the left hemisphere of S5, and bilaterally in S4, S6, and S7 compared with controls (Fig. 5 and Supplementary Fig. 5*A*,*B*).

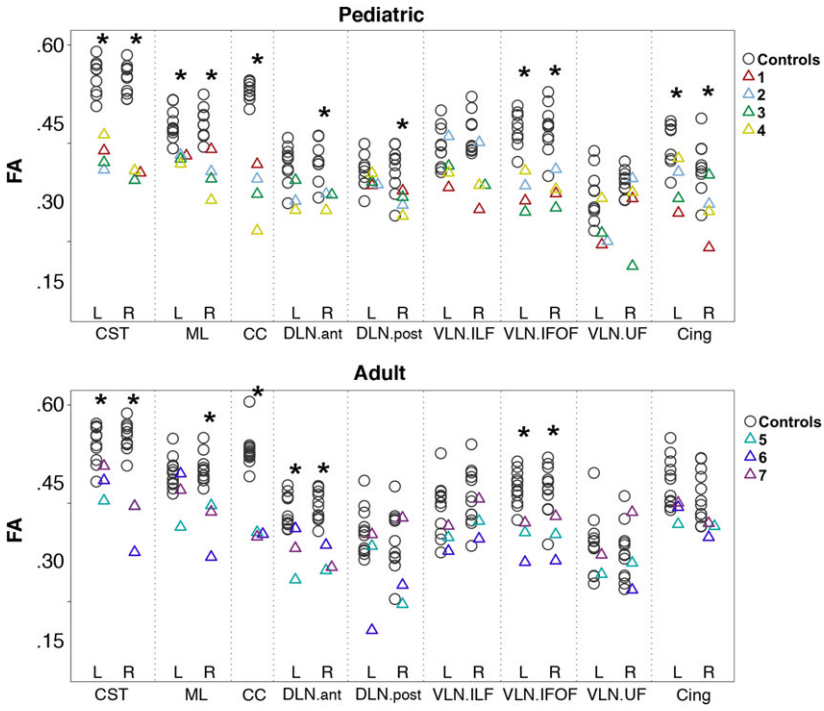


**Figure 2.** FA values of major white matter tracts. Scatter plots of FA value for major white matter tracts in pediatric and adult groups (*corrected $P < 0.05$). FA values are significantly lower for CST, ML, CC, right DLN.ant and right DLN.post VLN.IFOF, and cingulate-reconstructed tracts in the pediatric subjects compared with controls, and in the CST, CC, DLN.ant, VLN.IFOF, and right ML-reconstructed tracts in the adult subjects compared with controls. Note that the DTI sequence was performed with $b = 1000$ s/mm$^2$ in S1 and all of the pediatric controls. DTI was performed with $b = 700$ s/mm$^2$ for S2–S7 and all of the adult controls. CST = corticospinal tract, ML = medial lemniscus, CC = corpus callosum, DLN.ant = anterior segment of the dorsal language network, DLN.post = posterior segment of the dorsal language network, VLN.ILF = inferior longitudinal fasciculus of the ventral language network, VLN.IFOF = inferior fronto-occipital fasciculus of the ventral language network, VLN.UF = uncinate fasciculus of the ventral language network, Cing = cingulum.

All pediatric and adult controls had bilateral DLN.ant present, although they varied in fiber number (Supplementary Fig. 5A,B).

All pediatric and adult subjects had bilateral absence of the DLN.long, connecting inferior frontal areas with posterior superior/middle temporal areas (Fig. 5). By comparison, the DLN.long failed to reconstruct only in the right hemisphere of pediatric controls PC1 and PC6 (Supplementary Fig. 5A), in the right hemisphere of adult controls AC5, AC7, and AC2, and bilaterally in AC11 (Supplementary Fig. 5B).

The DLN.post was present in all pediatric and adult subjects but was shorter in S5 and S6 bilaterally (Fig. 5). The DLN.post was present in both pediatric and adult controls, except for AC10 right hemisphere, with variability in fiber number (Supplementary Figs. 5A,B).

Pediatric subjects had a significantly reduced FA in the right DLN.ant compared with pediatric controls ($P = 0.028$) and adult subjects had significantly reduced FA in the bilateral DLN.ant compared with adult controls ($P = 0.018$ for left DLN.ant and $P = 0.004$ for right DLN.ant) (Fig. 2). Pediatric subjects had a reduced FA for the right DLN.post compared with pediatric controls ($P = 0.024$) (Fig. 2).

There was no significant difference between the FA values of the adult subjects and the adult controls in the DLN.post bilaterally (Fig. 2). No statistical testing was performed for the DLN.long because it was missing bilaterally in all subjects.

*Ventral Language Network*. The VLN was reconstructed in all subjects except for the left VLN.UF in S6 (Fig. 6), and in all controls (Supplementary Fig. 6A,B). In pediatric subjects, bilateral VLN.IFOF were less compact and had significantly decreased mean FA compared with pediatric controls ($P = 0.002$ for left VLN.IFOF and $P = 0.004$ for right VLN.IFOF) (Fig. 2). Similarly in adult subjects, bilateral VLN.IFOF were less compact and had significantly decreased mean FA values compared with adult controls ($P = 0.004$ for left VLN.IFOF and $P = 0.018$ for right VLN.IFOF) (Fig. 2). There were no significant differences between subjects and controls' mean FA values of VLN.ILF and VLN.UF bilaterally (Fig. 2).

*Cingulum*. Tractography revealed a thinner Cing in most subjects, expect for left hemisphere of S4, S5, and S7, (Fig. 7) compared with most controls (Supplementary Fig. 7A,B). Mean FA was significantly decreased in the left and right Cing in pediatric subjects compared with controls ($P = 0.024$ and 0.024, respectively). Although mean FA was slightly decreased in adult subjects, the difference did not reach statistical significance (Fig. 2).

## Discussion

Here, we tested the neuropsychological profiles of and explored both brain structural and white matter organization in seven unrelated individuals who harbor identical de novo heterozygous *TUBB3* c.1228 G>A missense mutations. We found that the subjects' neuropsychological profiles include intellectual, language, social, and adaptive deficits of variable presentation and extent which, in isolation, are not diagnostic of a specific syndrome. By contrast, however, we identified a consistent aberrant trajectory of the CST to the posterior brainstem and bilateral absence of the DLN.long, as well as quantitatively

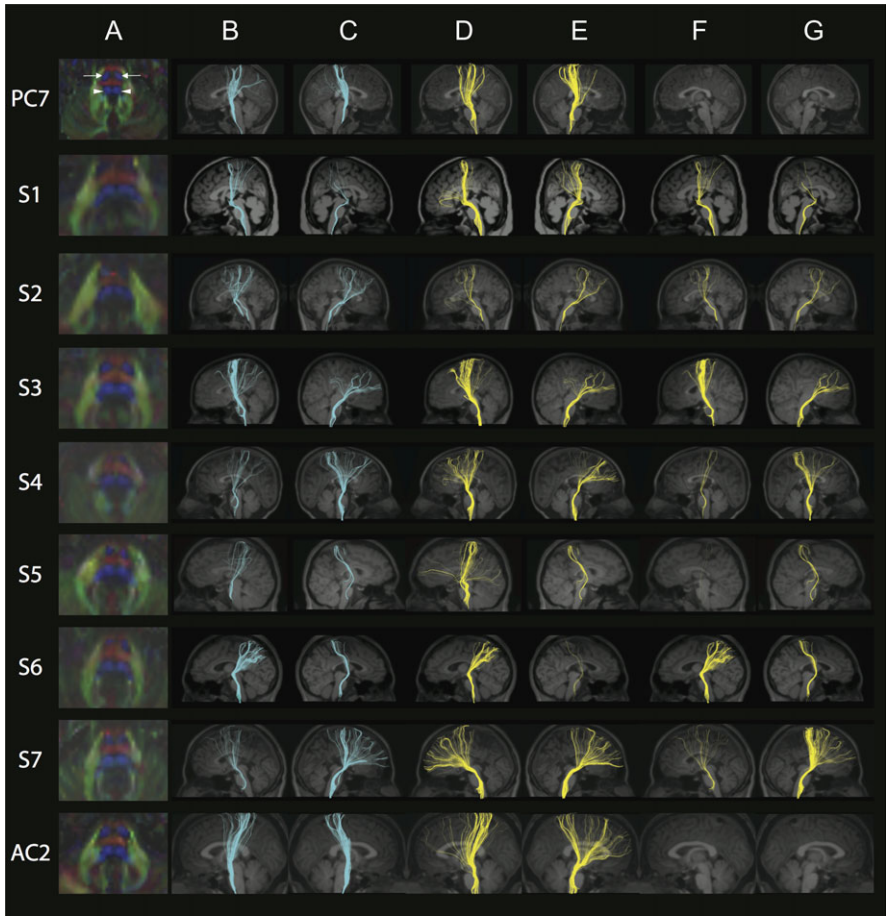


**Figure 3.** FA color maps, CST, and ML. Each row represents images for a single individual with row 1: pediatric control (PC7); rows 2–5: pediatric subjects S1–S4; rows 6–8: adult subjects S5–S7; row 9: adult control (AC2). The pseudocolored fibers are overlaid on each individual's coregistered sagittal MPRAGE shown in radiological convention in columns B–G. **Column A**: Axial FA color map of the midpons (typical radiological convention with left on the right and anterior at top of image), highlighting expected locations of pontine CST (bilateral anterior blue regions, anterior arrows in PC, column A) and pontine ML (bilateral posterior blue regions, posterior arrowheads in PC, column A). Note the variability in size and shape of the anterior and posterior blue regions in S1–S7 compared with controls. Color scheme represents the dominant direction of the principal eigenvector in each voxel; as per standard RGB convention for fiber direction, red corresponds to right/left, green corresponds to anterior posterior, and blue corresponds to superior/inferior. **Column B**: Fibers captured by one ROI placed in the left cerebral peduncle and another ROI in the ipsilateral anterior and posterior pons, anticipated to capture the left CST. **Column C:** Fibers captured by one ROI placed in the right cerebral peduncle and another ROI in the ipsilateral anterior and posterior pons, anticipated to capture the right CST. Note the variable CST reconstruction in subjects compared with controls in columns B and C. **Column D:** Fibers captured by an exclusion ROI placed in the left cerebral peduncle and an inclusion ROI placed in the ipsilateral anterior and posterior pons, anticipated to capture the left ML. **Column E**: Fibers captured by an exclusion ROI placed in the right cerebral peduncle and an inclusion ROI placed in the ipsilateral anterior and posterior pons, anticipated to capture the right ML. **Column F:** Fibers captured by two inclusions ROIs; one in the left cerebral peduncle and the other in the ipsilateral posterior pons. **Column G:** Fibers captured by two inclusions ROIs; one in the right cerebral peduncle and the other in the ipsilateral posterior pons. Note how in both columns F and G, there are no fibers captured in controls while subjects show abnormal tracts. See Supplementary Fig. 3A, *B* for pediatric and adult controls, respectively.

confirmed the qualitative findings of decreased CC volume (Tischfield et al. 2010; Chew et al. 2013). Abnormal white matter organization was evident in both pediatric and adult subjects as reduced network efficiency and increased path length. We also identified unexpected age-specific differences in pediatric and adult subjects compared with age-matched controls. These imaging findings extend previous qualitative studies describing small or absent CC and AntC in the TUBB3 E410K syndrome (Tischfield et al. 2010; Chew et al. 2013) and define a TUBB3 E410K neuroimaging endophenotype that includes age-related changes.

Given existing data supporting disrupted cranial nerve guidance and white matter organization in the TUBB3 E410K syndrome in humans and mice (Tischfield et al. 2010; Chew et al. 2013), we asked if subjects had evidence of aberrant axonal trajectories in the DTI tractography results. Surprisingly, only one subject showed suggestion of heterotopic CC connections. This is in contrast to the DTI findings reported in affected members of a family with CFEOM and polymicrogyria who segregated a *TUBB2B* mutation and had diffusion tractography evidence of heterotopic CC connections (Cederquist et al. 2012). Remarkably, however, we did identify an aberrant CST trajectory that was stereotypical and present bilaterally in all subjects: the CST coursed normally through the internal capsule and midbrain cerebral peduncle but then a large component deviated to run more posteriorly in the pons, merging with fibers of the ML. Despite the incorrect course of the CST, subjects had normal motor and sensory exams prior to the onset of a peripheral neuropathy as young adults. Thus, while our acquisitions did not extend low enough to assess medullary crossing of the CST, we predict that, similar to HGPPS (Amoiridis et al. 2006), CST axons successfully target the correct spinal cord level and motor

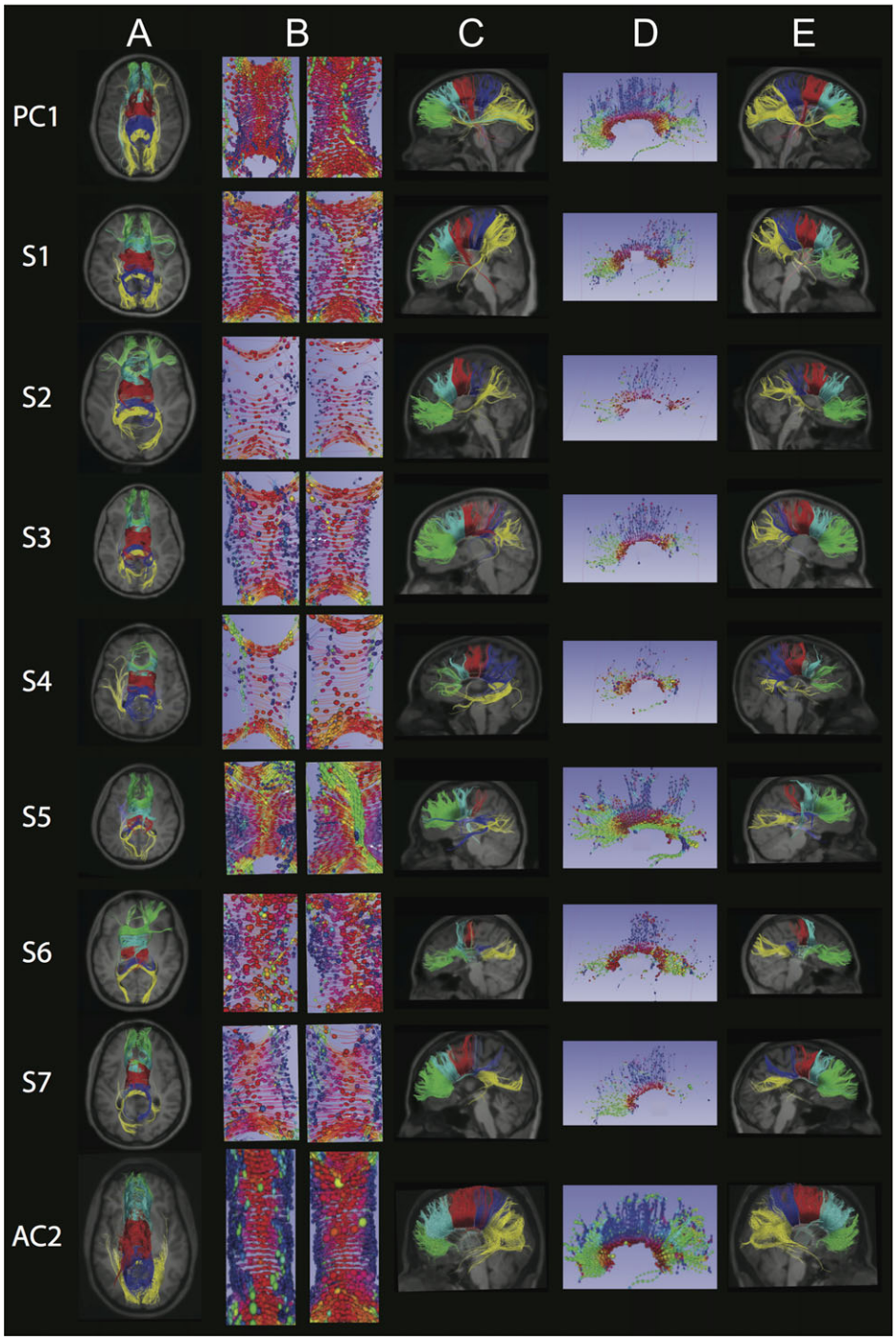


**Figure 4.** Corpus Callosum (CC): Each row represents images for a single individual with row 1: pediatric control (PC1); rows 2–5: pediatric subjects S1–S4; rows 6–8: adult subjects S5–S7; row 9: adult control (AC2). The pseudocolored fibers are overlaid on each individual's coregistered structural MPRAGE image presented in standard radiology convention in columns A and C. In column E, anterior is to the right. **Column A:** Axial view of five CC segments of equal length and psuedocolored as follows: green = anterior CC, turquoise = mid-anterior CC, red = central CC, dark blue = mid-posterior CC, yellow = posterior CC. **Column B:** Axial central segment of the CC from superior (left) and inferior (right) views, with ellipsoids showing orientation and organization of the fibers using standard RGB conventions for fiber direction. **Column C**: Left sagittal view of five pseudocolored CC segments as per column A. **Column D:** Sagittal view of the CC with anterior to the left and with ellipsoids showing orientation and organization of the fibers using standard RGB conventions for fiber direction. **Column E**: Right sagittal view of five pseudocolored CC segments as per columns A and C. **Columns B and D** created via 3D Slicer via the Slicer DMRI Project (dmri.slicer.org) (Norton et al. 2017). See Supplementary Fig. 4A,B for pediatric and adult controls, respectively.

neuron subtype, either contra- or ipsilaterally. Future DTI- and motor-evoked potential studies will resolve whether commissural crossing is perturbed. Tractography evidence of PF systems with incorrect trajectories has only been reported in one other patient with a TUBB3 but this was a TUBB3 MCD mutation. In this subject, dysmorphic internal capsules were noted with

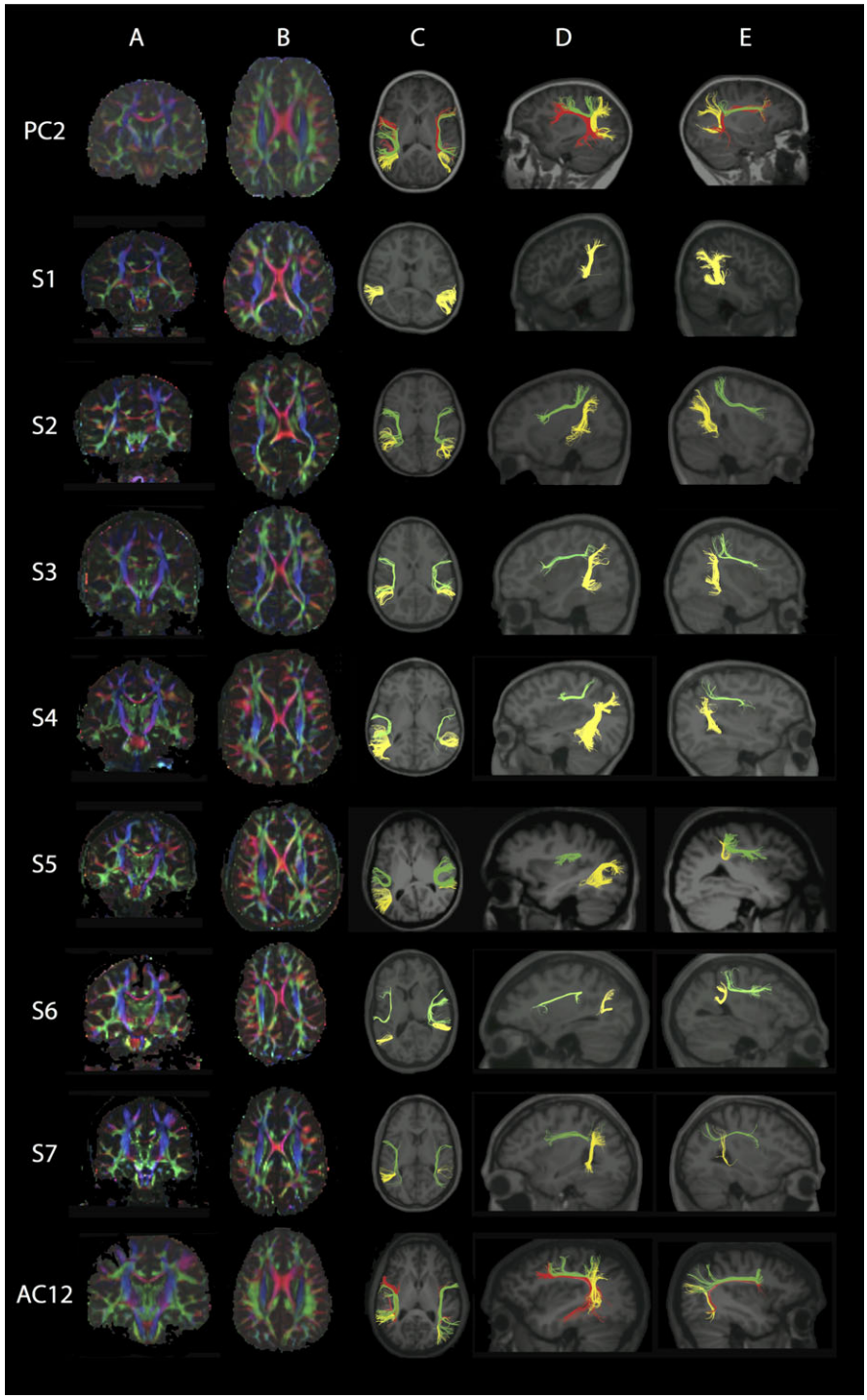


**Figure 5.** Dorsal Language Network (DLN). Each row represents images for a single individual with row 1: pediatric control (PC2); rows 2–5: pediatric subjects S1–S4; rows 6–8: adult subjects S5–S7; row 9: adult control (AC12). **Column A**: Coronal view of color FA maps at the level of the body of the CC (typical radiological convention with left on the right and anterior at top of image). **Column B:** Axial view of FA color maps at the level of the body of the CC. Note the absence of the DLN.long green region and smaller size of the DLN.ant green region in S1–S7 compared with controls. Color scheme represents the dominant direction of the principal eigenvector in each voxel; as per standard RGB convention for fiber direction, red corresponds to right/left, green corresponds to anterior posterior, and blue corresponds to superior/inferior. The pseudocolored fibers are overlaid on each individual's structural MPRAGE image, presented in standard radiological convention in columns C and D, while in column E anterior is to the right. **Column C:** Axial view showing the reconstructed segments of the DLN bilaterally; anterior segment (DLN.ant; green); long segment (DLN.long; red); posterior segment (DLN.post; yellow). **Column D:** Sagittal view of the left hemisphere shows reconstructed segments of the left DLN. **Column E:** Sagittal view of the right hemisphere shows reconstructed segments of the right DLN. Note that in all subjects the DLN.long could not be reconstructed. See Supplementary Fig. 5A,B for pediatric and adult controls, respectively.

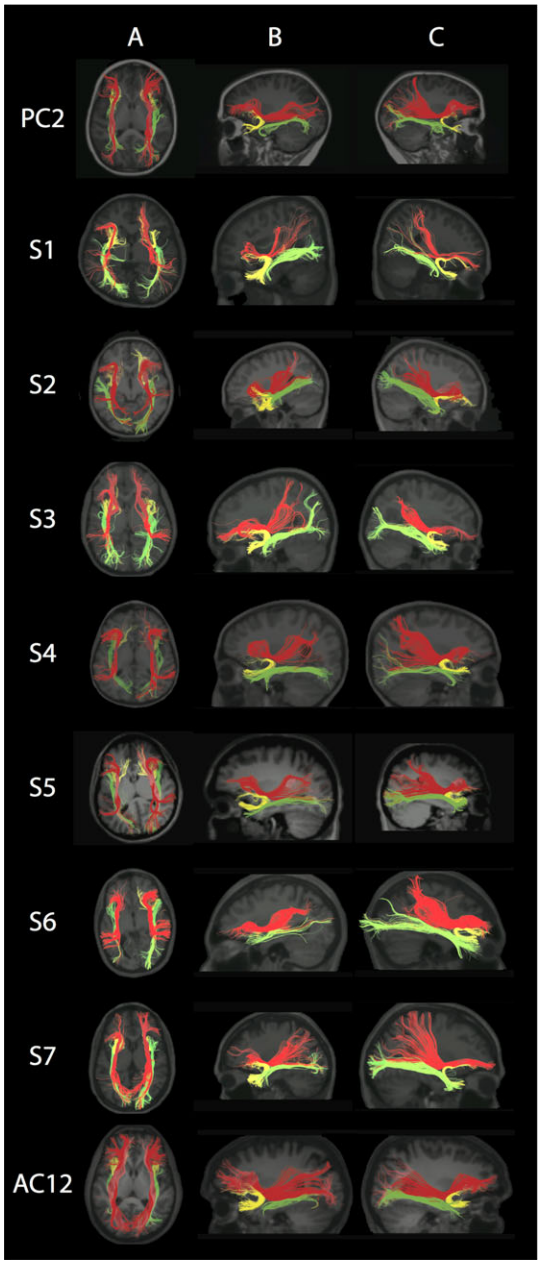


**Figure 6.** Ventral Language Network (VLN). Each row represents images for a single individual with row 1: pediatric control (PC2); rows 2–5: pediatric subjects S1–S4; rows 6–8: adult subjects S5–S7; row 9: adult control (AC12). The pseudocolored fibers are overlaid on each individual's' structural MPRAGE image, presented in standard radiological convention in columns A and B, while in column C, anterior is to the right. **Column A**: Axial view showing the bilateral inferior longitudinal fasciculus (VLN.ILF; green), inferior fronto-occipital fasciculus (VLN.IFOF; red), and uncinate fasciculus (VLN.UF; yellow). **Column B:** Left hemisphere showing the VLN. **Column C**: Right hemisphere showing the VLN. Note that fibers are more disorganized and in most cases fewer in number in subjects compared with controls. See Supplementary Fig. 6*A,B* for pediatric and adult controls, respectively.

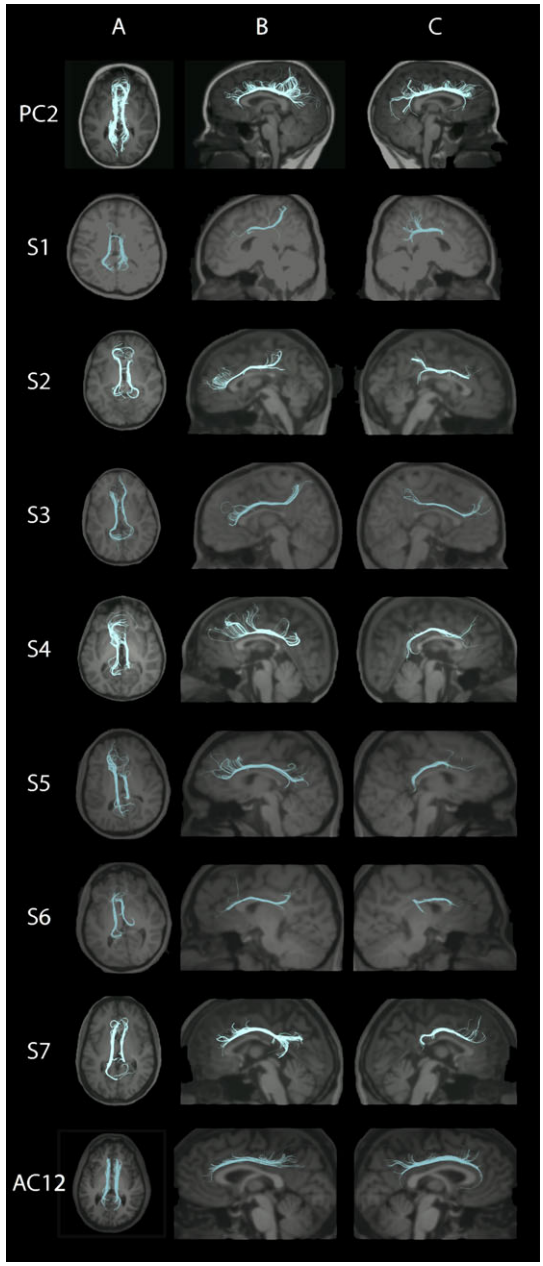


**Figure 7.** Cingulum. Each row represents images for a single individual with row 1: pediatric control (PC2); rows 2–5: pediatric subjects S1–S4; rows 6–8: adult subjects S5–S7; row 9: adult control (AC12). The pseudocolored fibers are overlaid on each individual's' structural MPRAGE image, presented in standard radiological convention in columns A and B, while in column C, anterior is to the right. **Column A**: Axial view of the Cing bilaterally. **Column B**: Left hemisphere showing the Cing. **Column C**: Right hemisphere showing the Cing. Note that fibers are more disorganized and in most cases fewer in number in subjects compared with controls. See Supplementary Fig. 7*A,B* for pediatric and adult controls, respectively.

what appear to be frontal PFs passing incorrectly through the posterior limb internal capsule (Poirier et al. 2010). The consistent aberrant course of the CST in TUBB3 E410K has not been previously reported.

Despite our identification of aberrant CC trajectories in subject S5, the asymptomatic aberrant trajectories of the CST in all subjects, and the higher quality of our DTI data compared with previous reports of axonal guidance disorders, we remained unable to identify deterministic tractography evidence of aberrant intrahemispheric axon trajectories. Surprisingly, aberrant trajectories of intrahemispheric white matter tracts have not been reported in human syndromes, including those ranging from malformations such as Aicardi Syndrome (Wahl et al.

2010) to developmental disorders such as autism (Ismail et al. 2016; Li et al. 2017). We did determine that subjects had smaller intrahemispheric tracts than controls, with consistent and complete absence of the DLN.long bilaterally. Notably, the number of reconstructed fibers is not a true measurement of axon count (Jones et al. 2013). Moreover, the clinical relevance and biological meaning of the inability to reconstruct DLN.long remains unclear: the DLN.long has a variable pattern of lateralization: 28–62.5% of typically developing controls were reported to be missing the right DLN.long (Catani et al. 2007; Verly et al. 2014; Ahtam et al. 2018), and 1/18 and 2/18 typically developing controls were reported to be missing the left DLN.ant and left DLN.long, respectively (Ahtam et al. 2018). Similar to other studies with MCD and bilateral absence of the DLN.long, four of the five subjects who underwent language evaluations in this study had significant language impairments (Bernal and Altman 2010; Bernal et al. 2010; Saporta et al. 2011; Kilinc et al. 2015; Paldino et al. 2016). Unlike subjects with MCD and bilateral absence of DLN.long reported by Paldino and Saporta, however, all of the TUBB3 E410K subjects had oral language (Saporta et al. 2011; Paldino et al. 2016). Notably, we observed bilateral absence of DLN.long in one adult control with intact language, although detailed language testing was not available. The milder language phenotype in TUBB3 E410K subjects and grossly intact language in this adult control could be due to the absence of frank MCD that was present in the prior studies or a compensatory role of the intact VLN (VLN was not assessed in the prior studies). Finally, the TUBB3 E410K subjects could have DLN axonal connections that could not be tracked due to abnormal fiber crossings or less compact axon bundles.

Although both pediatric and adult subjects showed evidence of altered white matter organization with decreased efficiency and increased path length, age- related changes were also identified. Pediatric subjects had no volumetric differences compared with pediatric controls but had significantly reduced whole-brain white matter mean FA, a clear bias to lower FA in longer range connections, and lower FA in the majority of the manually selection tracts. By contrast, adult subjects had significantly reduced brain surface area and white matter volume compared with adult controls but had no differences in whole-brain white matter mean FA, and had lower FA in fewer manually selected tracts. It is intriguing that white matter-decreased FA was a more prominent feature in pediatric subjects, while white matter volume loss was present only in adult subjects. These findings suggest that the imaging phenotype in TUBB3 E410K brains undergoes modification from teenage to adult years. The more consistent low FA in the pediatric subjects could represent less compact axonal tracts due to misguidance. The loss of white matter volume and less significant decreases in FA in adults suggests a loss of axonal connectivity over time, possibly due to regression of less compact, misguided axons. Increasing myelination could also increase FA (Hagmann et al. 2010) but such a process should be associated with stable to increased rather than decreased white matter volumes. Thus, we hypothesize that misguided axons contribute to decreased FA in children, and with maturation these misguided axons regress, leading to white matter volume loss and less pronounced FA decreases in adult subjects. We also cannot exclude other genetic or environmental factors causing changes over time, but the robust and consistent differences between all pediatric and all adult subjects related to age-matched controls supports an etiology related to their common genotype.

Cortical surface area was decreased only in adults, which suggests altered scaling with brain growth in TUBB3 E410K subjects. Previous human and interspecies studies have shown a higher ratio of white matter to whole-brain volumes as brain size increases, with an associated dramatic increase in cortical surface area (Zhang and Sejnowski 2000; Im et al. 2008). It has been hypothesized that the relative expansion of white matter compared with gray matter is favored in larger brains to support increased white matter connections in response to the increased number of neurons. The decreased cortical surface area observed only in the TUBB3 E410K adult subjects relative to adult controls also supports the hypothesis of decreased white matter connectivity developing with increasing age. However, future longitudinal studies and immunohistochemical validation are needed.

Although this is one of the largest MRI tractography studies of a single fully penetrant genetic disorder, it remains limited by small subject numbers and inconsistent diffusion acquisitions. As noted previously, although *b* values were inconsistent in the pediatric group, the major metric we analyzed was FA, which has been shown to exhibit little change over the ranges used in this study. In addition, all subjects and adult controls had 60 direction DTI acquisitions, whereas the pediatric controls had only 30 direction DTI acquisitions. This increased number of diffusion directions in pediatric subjects compared with pediatric controls would, however, result in higher signal-to-noise and bias the results to more, rather than fewer, tracts being reconstructed in the subjects.

Few diffusion tractography and quantitative volumetric analysis studies in axonal guidance disorders have been reported and where reports exist, they are typically in genetically heterogeneous populations with a spectrum of MR imaging endophenotypes. Here, we provide a detailed qualitative and quantitative analysis of seven subjects with de novo *TUBB3* c.1228 G>A missense mutations who present with the resulting fully penetrant TUBB3 E410K human syndrome and report a MR imaging endophenotype with age-related changes and ipsilateral misguidance of the CST. However, despite their social and intellectual disabilities, we did not discover deterministic tractography evidence of misguided intrahemispheric connections. This is a common theme among many social and intellectual disorders thought to result from altered intrahemispheric corticocortical connections. We hypothesize that, unlike compact misguided interhemispheric and projection axons, ipsilateral intracortical misguided connections may not be supported, or do not occur at the level of macroscopic bundles. It is possible that intracortical misguidance results in decreased compactness of the typical axonal bundles and, therefore, only decreased FA is detectable at the millimeter resolution of diffusion tractography. The changes with age in our subjects support this hypothesis, but future animal and human autopsy studies are required to confirm it.

## Supplementary Material

Supplementary material is available at *Cerebral Cortex* online.

## Funding

National Institutes of Health NEI R01EY12498 (ECE) and the Boston Children's Hospital IDDRC (1U54HD090255).

## Notes

The authors thank the families for their participation and members of the Engle lab for their technical assistance and discussions. The authors also thank Randy Gollub for providing normal adult controls and Rudolph Pienaar for assistance in image data management. ECE is an investigator of the Howard Hughes Medical Institute. *Conflict of Interest*: None declared.

## References

Ahtam B, Link N, Hoff E, Ellen Grant P, Im K. 2018. Altered structural brain connectivity involving the dorsal and ventral language pathways in 16p11.2 deletion syndrome. Brain Imaging Behav. doi:10.1007/s11682-018-9859-3.

Amoiridis G, Tzagournissakis M, Christodoulou P, Karampekios S, Latsoudis H, Panou T, Simos P, Plaitakis A. 2006. Patients with horizontal gaze palsy and progressive scoliosis due to ROBO3 E319K mutation have both uncrossed and crossed central nervous system pathways and perform normally on neuropsychological testing. J Neurol Neurosurg Psychiatry. 77:1047–1053.

Bahi-Buisson N, Poirier K, Fourniol F, Saillour Y, Valence S, Lebrun N, Hully M, Bianco CF, Boddaert N, Elie C, et al. 2014. The wide spectrum of tubulinopathies: what are the key features for the diagnosis? Brain. 137:1676–1700.

Basser PJ, Mattiello J, LeBihan D. 1994. MR diffusion tensor spectroscopy and imaging. Biophys J. 66:259–267.

Benjamini Y, Hochberg Y. 1995. Controlling the false discovery rate: a practical and powerful approach to multiple testing. J R Stat Soc Ser B. 57:289–300.

Bernal B, Altman N. 2010. The connectivity of the superior longitudinal fasciculus: a tractography DTI study. Magn Reson Imaging. 28:217–225.

Bernal B, Rey G, Dunoyer C, Shanbhag H, Altman N. 2010. Agenesis of the arcuate fasciculi in congenital bilateral perisylvian syndrome: a diffusion tensor imaging and tractography study. Arch Neurol. 67:501–505.

Catani M, Allin MP, Husain M, Pugliese L, Mesulam MM, Murray RM, Jones DK. 2007. Symmetries in human brain language pathways correlate with verbal recall. Proc Natl Acad Sci USA. 104:17163–17168.

Catani M, Thiebaut de Schotten M. 2008. A diffusion tensor imaging tractography atlas for virtual in vivo dissections. Cortex. 44:1105–1132.

Cederquist GY, Luchniak A, Tischfield MA, Peeva M, Song Y, Menezes MP, Chan WM, Andrews C, Chew S, Jamieson RV, et al. 2012. An inherited TUBB2B mutation alters a kinesin-binding site and causes polymicrogyria, CFEOM and axon dysinnervation. Hum Mol Genet. 21:5484–5499.

Chew S, Balasubramanian R, Chan WM, Kang PB, Andrews C, Webb BD, MacKinnon SE, Oystreck DT, Rankin J, Crawford TO, et al. 2013. A novel syndrome caused by the E410K amino acid substitution in the neuronal beta-tubulin isotype 3. Brain. 136:522–535.

Chung MK, Robbins SM, Dalton KM, Davidson RJ, Alexander AL, Evans AC. 2005. Cortical thickness analysis in autism with heat kernel smoothing. Neuroimage. 25:1256–1265.

Dale AM, Fischl B, Sereno MI. 1999. Cortical surface-based analysis. I. Segmentation and surface reconstruction. Neuroimage. 9:179–194.

Desikan RS, Segonne F, Fischl B, Quinn BT, Dickerson BC, Blacker D, Buckner RL, Dale AM, Maguire RP, Hyman BT, et al. 2006. An automated labeling system for subdividing the human cerebral cortex on MRI scans into gyral based regions of interest. Neuroimage. 31:968–980.

Fischl B, Sereno MI, Dale AM. 1999. Cortical surface-based analysis. II: inflation, flattening, and a surface-based coordinate system. Neuroimage. 9:195–207.

Fischl B, van der Kouwe A, Destrieux C, Halgren E, Segonne F, Salat DH, Busa E, Seidman LJ, Goldstein J, Kennedy D, et al. 2004. Automatically parcellating the human cerebral cortex. Cereb Cortex. 14:11–22.

Genovese CR, Lazar NA, Nichols T. 2002. Thresholding of statistical maps in functional neuroimaging using the false discovery rate. Neuroimage. 15:870–878.

Hagmann P, Sporns O, Madan N, Cammoun L, Pienaar R, Wedeen VJ, Meuli R, Thiran JP, Grant PE. 2010. White matter maturation reshapes structural connectivity in the late developing human brain. Proc Natl Acad Sci USA. 107: 19067–19072.

Hui ES, Cheung MM, Chan KC, Wu EX. 2010. B-value dependence of DTI quantitation and sensitivity in detecting neural tissue changes. Neuroimage. 49:2366–2374.

Im K, Ahtam B, Haehn D, Peters JM, Warfield SK, Sahin M, Ellen Grant P. 2016. Altered structural brain networks in tuberous sclerosis complex. Cereb Cortex. 26:2046–2058.

Im K, Jo HJ, Mangin JF, Evans AC, Kim SI, Lee JM. 2010. Spatial distribution of deep sulcal landmarks and hemispherical asymmetry on the cortical surface. Cereb Cortex. 20:602–611.

Im K, Lee JM, Lyttelton O, Kim SH, Evans AC, Kim SI. 2008. Brain size and cortical structure in the adult human brain. Cereb Cortex. 18:2181–2191.

Im K, Paldino MJ, Poduri A, Sporns O, Grant PE. 2014. Altered white matter connectivity and network organization in polymicrogyria revealed by individual gyral topology-based analysis. Neuroimage. 86:182–193.

Ismail MM, Keynton RS, Mostapha MM, ElTanboly AH, Casanova MF, Gimel'farb GL, El-Baz A. 2016. Studying autism spectrum disorder with structural and diffusion magnetic resonance imaging: a survey. Front Hum Neurosci. 10:211.

Jenkinson M, Bannister P, Brady M, Smith S. 2002. Improved optimization for the robust and accurate linear registration and motion correction of brain images. Neuroimage. 17: 825–841.

Jones DK, Knosche TR, Turner R. 2013. White matter integrity, fiber count, and other fallacies: the do's and don'ts of diffusion MRI. Neuroimage. 73:239–254.

Keays DA, Tian G, Poirier K, Huang GJ, Siebold C, Cleak J, Oliver PL, Fray M, Harvey RJ, Molnar Z, et al. 2007. Mutations in alpha-tubulin cause abnormal neuronal migration in mice and lissencephaly in humans. Cell. 128:45–57.

Kilinc O, Ekinci G, Demirkol E, Agan K. 2015. Bilateral agenesis of arcuate fasciculus demonstrated by fiber tractography in congenital bilateral perisylvian syndrome. Brain Dev. 37: 352–355.

Latora V, Marchiori M. 2001. Efficient behavior of small-world networks. Phys Rev Lett. 87:198701.

Lazar M. 2010. Mapping brain anatomical connectivity using white matter tractography. NMR Biomed. 23:821–835.

Li D, Karnath HO, Xu X. 2017. Candidate biomarkers in children with autism spectrum disorder: a review of MRI studies. Neurosci Bull. 33:219–237.

Lopata MA, Cleveland DW. 1987. In vivo microtubules are copolymers of available beta-tubulin isotypes: localization of each of six vertebrate beta-tubulin isotypes using polyclonal antibodies elicited by synthetic peptide antigens. J Cell Biol. 105:1707–1720.

Maslov S, Sneppen K. 2002. Specificity and stability in topology of protein networks. Science. 296:910–913.

Melhem ER, Itoh R, Jones L, Barker PB. 2000. Diffusion tensor MR imaging of the brain: effect of diffusion weighting on trace and anisotropy measurements. AJNR Am J Neuroradiol. 21:1813–1820.

Niwa S, Takahashi H, Hirokawa N. 2013. beta-Tubulin mutations that cause severe neuropathies disrupt axonal transport. EMBO J. 32:1352–1364.

Norton I, Essayed W, Zhang F, Pujol S, Yarmarkovich A, Golby AJ, Kindlmann G, Wassermann D, Estepar RSJ, Rathi Y, et al. 2017. SlicerDMRI: open source diffusion MRI software for brain cancer research. Cancer Res. 77: e101–e103.

Oegema R, Cushion TD, Phelps IG, Chung SK, Dempsey JC, Collins S, Mullins JG, Dudding T, Gill H, Green AJ, et al. 2015. Recognizable cerebellar dysplasia associated with mutations in multiple tubulin genes. Hum Mol Genet. 24: 5313–5325.

Onnela JP, Saramaki J, Kertesz J, Kaski K. 2005. Intensity and coherence of motifs in weighted complex networks. Phys Rev E Stat Nonlin Soft Matter Phys. 71:065103.

Paldino MJ, Hedges K, Golriz F. 2016. The arcuate fasciculus and language development in a cohort of pediatric patients with malformations of cortical development. AJNR Am J Neuroradiol. 37:169–175.

Poirier K, Saillour Y, Bahi-Buisson N, Jaglin XH, Fallet-Bianco C, Nabbout R, Castelnau-Ptakhine L, Roubertie A, Attie-Bitach T, Desguerre I, et al. 2010. Mutations in the neuronal ss-tubulin subunit TUBB3 result in malformation of cortical development and neuronal migration defects. Hum Mol Genet. 19:4462–4473.

Radmanesh A, Zamani AA, Whalen S, Tie Y, Suarez RO, Golby AJ. 2015. Comparison of seeding methods for visualization of the corticospinal tracts using single tensor tractography. Clin Neurol Neurosurg. 129:44–49.

Rubinov M, Sporns O. 2010. Complex network measures of brain connectivity: uses and interpretations. Neuroimage. 52:1059–1069.

Saporta AS, Kumar A, Govindan RM, Sundaram SK, Chugani HT. 2011. Arcuate fasciculus and speech in congenital bilateral perisylvian syndrome. Pediatr Neurol. 44: 270–274.

Schmahmann JD, Pandya DN. 2009. Fiber pathways of the brain. New York, NY: Oxford University Press.

Shukla DK, Keehn B, Smylie DM, Muller RA. 2011. Microstructural abnormalities of short-distance white matter tracts in autism spectrum disorder. Neuropsychologia. 49:1378–1382.

Sporns O, Tononi G, Kotter R. 2005. The human connectome: A structural description of the human brain. PLoS Comput Biol. 1:e42.

Ti SC, Pamula MC, Howes SC, Duellberg C, Cade NI, Kleiner RE, Forth S, Surrey T, Nogales E, Kapoor TM. 2016. Mutations in human tubulin proximal to the kinesin-binding site alter dynamic instability at microtubule plus- and minus-ends. Dev Cell. 37:72–84.

Tischfield MA, Baris HN, Wu C, Rudolph G, Van Maldergem L, He W, Chan WM, Andrews C, Demer JL, Robertson RL, et al. 2010. Human TUBB3 mutations perturb microtubule dynamics, kinesin interactions, and axon guidance. Cell. 140:74–87.

Verly M, Verhoeven J, Zink I, Mantini D, Van Oudenhove L, Lagae L, Sunaert S, Rommel N. 2014. Structural and functional underconnectivity as a negative predictor for language in autism. Hum Brain Mapp. 35:3602–3615.

Wahl M, Strominger ZA, Wakahiro M, Jeremy RJ, Mukherjee P, Sherr EH. 2010. Diffusion tensor imaging of Aicardi syndrome. Pediatr Neurol. 43:87–91.

Wakana S, Jiang H, Nagae-Poetscher LM, van Zijl PC, Mori S. 2004. Fiber tract-based atlas of human white matter anatomy. Radiology. 230:77–87.

Wang R, Beener T, Sorensen AG, Wedeen VJ. 2007. Diffusion toolkit: a software package for diffusion imaging data processing and tractography. Proc Intl Soc Mag Reson Med. 15:3720.

Watts DJ, Strogatz SH. 1998. Collective dynamics of 'small-world' networks. Nature. 393:440–442.

Whitman MC, Andrews C, Chan WM, Tischfield MA, Stasheff SF, Brancati F, Ortiz-Gonzalez X, Nuovo S, Garaci F, MacKinnon SE, et al. 2016. Two unique TUBB3 mutations cause both CFEOM3 and malformations of cortical development. Am J Med Genet A. 170A:297–305.

Yendiki A, Koldewyn K, Kakunoori S, Kanwisher N, Fischl B. 2013. Spurious group differences due to head motion in a diffusion MRI study. Neuroimage. 88C:79–90.

Zhang K, Sejnowski TJ. 2000. A universal scaling law between gray matter and white matter of cerebral cortex. Proc Natl Acad Sci USA. 97:5621–5626.